Observation and analysis of interactive phenomena between microbubbles and underwater shock wave

Abe, A.

Wang, J.

Shioda, M.

Maeno, S.

(Citation)
Journal of Visualization, 18(3):437-447

(Issue Date)
2015-08

(Resource Type)
journal article

(Version)
Accepted Manuscript

Observation and analysis of interactive phenomena between microbubbles and underwater shock wave

A. ABE[1C], J. WANG[1], M. SHIODA[1], S. MAENO[1]

[1] Graduate School of Maritime Sciences, Kobe University, Kobe 658-0022, Japan
[C]Corresponding author: Tel.: +81784316277; Fax: +81784316277; Email: a-abe@maritime.kobe-u.ac.jp

Abstract
This paper reports the observation and analysis of the microbubble motion induced by an underwater shock wave. In the analysis, Herring's bubble motion equation was numerically solved using an experimental shock wave pressure profile. The pressure attenuation of the rebound shock wave of a microbubble was also estimated by numerical simulation. The motion behaviors of the microbubbles during their interaction with an electric discharge shock wave, such as their rebound, shock wave generation, and microjet formation, were observed by magnified visualization. To improve the observation accuracy, spatial positioning control of the microbubbles was employed. The experimentally determined time variation of the diameter of the microbubbles when they collapsed spherically was in agreement with the results of the numerical analyses, and the latter also revealed a very high pressure of the rebound shock wave. There were, however, discrepancies between the experimental and analytical results for non-spherical collapse. It is thought that spherical collapse produces stronger rebound shock waves and that the probability of such collapse increases with decreasing diameter of the bubble. In addition, it was demonstrated that single and multiple microbubbles moved vigorously after interaction with a shock wave and the latter coalesced into a single bubble within several hundred microseconds.

Keywords: Microbubble, Shock wave interaction, Rebound shock wave, Microjet, Enlarged observation, Microscopic observation, Numerical analysis

1. Introduction

The application of microbubbles has been extensively studied in recent times, including in the fields of biomedical engineering, civil engineering, and fishing. In the area of maritime science, the shock waves generated by the collapse of microbubbles have been studied for application to killing bacteria in the ballast water of a ship [1]. The discharged ballast water of a ship contains bacteria of a foreign origin, and this could be destructive to the local marine ecosystem and create a global environmental problem. Toward conservation of marine environment, the International Maritime Organization (IMO) established the International Convention for the Control and Management of Ships' Ballast Water and Sediments [2]. The enforcement of the convention treaty would necessitate ballast water treatment. In general treatment systems, large creatures and suspended solid particles are physically removed from the ballast water by filters, and the remaining microorganisms are chemically killed by the addition of acid carbon dioxide or chlorine dioxide [3]. However, the use of chemicals onboard is risky and also raises some challenges. For instance, the chemicals need to be stored and managed, and this increases the cargo dead space. Furthermore, if the chemicals are accidentally discharged into the sea, they would pollute the marine ecosystem and may cause secondary disasters.

Abe et al. [4] proposed a new method for ship ballast water treatment, in which free radicals and shock waves produced by collapsing microbubbles are used to kill the bacteria without the application of chemicals. They experimentally confirmed the sterilization effects of this method on marine *Vibrio* sp. using microbubbles exposed to shock waves. To establish this water treatment technique, it is important to understand the behavior of microbubbles after interaction with external shock waves, and determine the optimum conditions with regard to the relationship between the size of the microbubbles and the pressure of the shock waves. However, it is difficult to observe the motion of microbubbles owing to their very small size and the very high propagation velocity of underwater shock wave.

This paper reports the observation and analysis of interactive phenomena between microbubbles and underwater shock waves. In the experiment, the microbubbles were produced by air trapped in salt crystals [5], and the underwater shock waves used to induce the movement of the microbubbles were generated by electric discharge. An ultra-high-speed framing camera was used to observe and obtain images of the contraction and expansion of the microbubbles. To improve the observation accuracy, spatial positioning control of the microbubbles was employed. The experimental observation was used to determine whether the collapse motion of the bubbles was symmetrical or unsymmetrical. In the case of symmetrical motion, it was possible to compare the experimental results with the analytical solutions, which were obtained by a one-dimensional point-symmetric model based on Herring's bubble equation [6] and the experimental pressure profiles of the external shock waves. Furthermore, the pressures of the rebound shock waves were estimated by a total-variation-diminishing (TVD) finite-difference scheme using the analytical bubble surface velocity variation as the boundary condition. The behaviors of a single bubble and multiple bubbles after interaction with shock waves were also observed.

2. Theoretical Analysis

2.1 Analysis of Microbubble Motion Equation

A one-dimensional point-symmetric bubble model was used to analyze the spherical collapse motion of the microbubbles. Considering the small volume of the microbubble, the vapor gas was ignored in the model, and the model bubble was therefore assumed to be filled with perfect non-conducting non-viscous non-condensable gas. A spherical gas bubble of radius R was considered to be at rest in an infinite volume of compressible liquid. The bubble began to shrink and the internal pressure increased when an external shock wave passed through it. The rebound shock wave was generated just after the bubble began to expand from its minimum radius. The bubble was assumed to maintain a spherical shape during the contraction and expansion of the collapse motion.

Taking into consideration the compressibility of the liquid, Herring's bubble motion equation was solved by using a fourth-order Gill-Runge-Kutta method [7] to numerically analyze the collapse motion of the microbubble induced by the shock wave. In the equation, the acoustical approximate was considered to assume the constant velocity of sound in the liquid [6]. Herring's equation was written as

$$\left(1-\frac{2\dot{R}}{C_\infty}\right)R\ddot{R}+\frac{3}{2}\left(1-\frac{4}{3}\frac{\dot{R}}{C_\infty}\right)\dot{R}^2+\frac{1}{\rho_\infty}\left(P_\infty-P_s-\frac{R}{C_\infty}\frac{dP_s}{dt}\right)=0 \tag{1}$$

where R is the radius of a bubble, R_0 is the initial bubble radius, C_∞ is the speed of sound in the liquid at an infinite distance, ρ_∞ is the density of the liquid at an infinite distance, P_s is the pressure at a bubble wall, P_∞ is the external pressure behind the induced shock wave. C_∞ is given by

$$C_\infty=\sqrt{\frac{n(P_\infty+B)}{\rho_\infty}}, \tag{2}$$

where B and n are constant values, B = 2963 bar, n = 7.41.

P_s in Eq. (1) is written by

$$P_s=P_{in}-\frac{1}{R}\left(2\sigma+4\mu\dot{R}\right), \tag{3}$$

where P_{in} is the pressure inside a bubble, μ is the coefficient of viscosity of the liquid, σ is the surface tension of the liquid. P_{in} is described by

$$P_{in}=P_l+P_g=P_l+P_{g0}\left(\frac{R_0}{R}\right)^{3\gamma}, \tag{4}$$

where P_l is the pressure of the vapor gas in a bubble, P_g is the pressure of the non-condensable gas in the bubble, P_{g0} is the initial pressure of the non-condensable gas in the bubble, γ is the specific heats ratio of the gas inside the bubble. In the analysis, the vapor inside the bubble is ignored. Thus, Eq. (3) is rewritten as

$$P_s=P_{g0}\left(\frac{R_0}{R}\right)^{3\gamma}-\frac{1}{R}\left(2\sigma+4\mu\dot{R}\right). \tag{5}$$

At the initial condition, we assume that radius R is R_0 and the pressure P_s is the standard atmospheric pressure P_0 in Eq. (3). Then, P_{g0} is given by

$$P_{g0}=P_0+\frac{2\sigma}{R_0}. \tag{6}$$

Fig. 1 shows the experimental profile of a spherical shock wave measured at 60 mm from the discharge point. In the analysis, the pressure profile shown in Fig. 1 was substituted into P_∞ in Herring's bubble motion equation to predict the contraction and expansion motion of a bubble. Fig. 2 shows the time variations of the bubble diameter and internal pressure for initial bubble diameters of 10, 30, and 50 μm, as analytically determined using Eq. (1). As shown in Fig. 2, the time required for the bubble to shrink to the minimum diameter increases with increasing initial diameter. This suggests that the maximum internal pressure of the bubble is not proportional to the initial diameter of the bubble for a given shock wave strength. Fig. 3 shows the relationship between the maximum internal pressure of the bubble and the initial bubble diameter when the bubble motion is induced by a shock wave of a given strength. It can be seen that the estimated internal pressures are several hundred MPa, and the maximum pressure corresponds to a particular initial bubble diameter for the pressure profile of the external shock wave. In this case, it is predicted that a maximum pressure of over 700 MPa would be obtained for a small initial bubble diameter of about 25 μm. This is because a small bubble contracts quickly and begins to expand before the pressure around it is sufficiently high. Conversely, if the bubble is large, longer time would be required for the contraction and the pressure around bubble would attain the peak value and begin to decrease before the bubble sufficiently contracts. The forgoing indicates that, to obtain a high internal pressure in the bubbles, it is necessary to select an initial bubble diameter suitable for the pressure profile of the induced shock waves.

2.2 Estimation of Rebound Shock Pressure

Although the results in Fig. 3 suggest that the optimal range of the bubble diameter to achieve a maximum internal pressure of about 700 MPa is 20–30 μm, the strength of the rebound shock wave produced by the microbubble motion was not estimated in the above analysis. Although the pressure variation of the rebound shock waves is of great interest, it is difficult to measure owing to its rapid attenuation within a very small region. To numerically estimate the pressure attenuation, a point-symmetric numerical simulation scheme based on the variation of the surface velocity and diameter of a bubble obtained by analysis using Herring's bubble motion equation was developed. The fundamental equations of the simulation that was performed are as follows

$$U_t + F(U)_r = -G(U), \qquad (7)$$

where U is the vector of the conservative variables, F is the flux vector, and G is the attenuation vector. The vectors are given by the following matrixes:

$$U = \begin{bmatrix} \rho \\ \rho u \end{bmatrix}, F(U) = \begin{bmatrix} \rho u \\ P + \rho u^2 \end{bmatrix}, G(U) = \frac{2}{r}\begin{bmatrix} \rho u \\ \rho u^2 \end{bmatrix}, \qquad (8)$$

where ρ is the density of the water, u is the water velocity in the radial direction, P is the pressure, and r is the radial coordinate.

The Tait equation was used as the equation of state of the water, and is written as

$$\frac{P + B}{P_0 + B} = \left(\frac{\rho}{\rho_0}\right)^n, \qquad (9)$$

where B and n are constants (B = 2963 bar, n = 7.41). In the present numerical simulation, equation (7) was solved by a second-order accurate explicit TVD finite-difference scheme of the Harten-Yee type [8].

In the simulation, the analytical data of the bubble surface velocity obtained by Herring's equation were substituted into the numerical scheme as the boundary conditions. Additionally, the initial pressure and density of the water around a bubble were set using the normalized pressure profile of the external shock wave shown in Fig. 1. The initial particle velocity in the water was assumed to be zero because it appeared to be much smaller than the bubble surface velocity. The computational grids were reconstructed at every computational time step to increase the computation accuracy with respect to the bubble motion. In other words, the grid size at every time step was set in accordance with the analytical solution of the bubble radius. Consequently, during the shrinking of a bubble, the resolution of the calculation increased with decreasing grid size. Conversely, the resolution decreased during the expansion of the bubble. However, it was thought that the loss of resolution during bubble expansion had no effect on the results of the investigation of the rebound shock wave behavior because the size of the microbubble remained sufficiently small.

Fig. 4 shows the numerical pressure attenuation curves of the first rebound shock waves generated by microbubbles of diameters 10, 30, and 50 μm exposed to the incident shock wave shown in Fig. 1. The horizontal axis of Fig. 4 represents the distance in the radial direction from the center of the microbubble, and the starting points of the pressure curves correspond to the respective radii of the microbubbles at the instant that the rebound shock wave front was generated. Comparison of the changes in bubble diameter determined by the analysis in Section 2.1 with the results in Fig. 4 reveals that the bubble radii at the generation of the rebound shock wave are a little larger than the minimum radii. The maximum pressures of the rebound shock waves are also higher than the internal pressures estimated in Section 2.1. Furthermore, as predicted by Fig. 3, the maximum rebound shock wave pressure corresponds to an initial bubble diameter of 30 μm.

3. Experimental Observations and Discussion

3.1 Visualization of Microbubble Collapse

3.1.1 Observation method and procedure

Fig. 5 is a schematic of the experimental water tank, which comprised three components: the shock wave generation unit (SU), the microbubble position control unit (MU), and the buffer unit (BU). The components were separated by silicone films of thickness 0.1 mm. Electrode holes were made in the SU 20 mm from the observation point in the MU. The BU was used as a shield against the effect of the reflected shock wave. Water inlet and outlet holes were also made in the backside of the MU to allow down flow, and the flow rate could be adjusted by a valve in the drainage pipe. When the floating speed of the microbubbles equaled the down flow speed, the microbubbles could remain near the observation point. In addition, the horizontal position of the microbubbles was manipulated by tilting the goniometer stage. The positioning operations were used to trap the microbubbles in the focus area for photographing.

Fig. 6 is a schematic of the optical arrangement for visualizing the collapse motion of a microbubble using an ultra-high-speed framing camera. The experimental setup consists of the ultra-high-speed framing camera, an oscilloscope, a fiber optical probe hydrophone (FOPH2000, PR Acoustics Co.), a focus adjustment camera, a flash light source, a metal halide lamp (LS-M350, SUMITA Optical glass Inc.), a function generator, and a high-voltage pulse discharge power supply for generating an underwater shock wave. Two types of ultra-high-speed framing cameras (SIM, Specialized Imaging Co.; and ULTRA Neo, Nac Image Technology Co.) were used for the experiment. The observation point in the MU was first decided by focusing the focus adjustment camera and the ultra-high-speed framing camera on each other. The salt crystals in which air was trapped were then put in the MU to generate the microbubbles. When a microbubble moved upward due to the buoyant force, it was manipulated by the goniometer and the valve of the drainage pipe to maintain its position in the preset focus of the focus adjustment camera. The focus adjustment camera was thereafter replaced by the flash lamp, which had a pinhole [9], and the experimental observation by the ultra-high-speed framing camera was commenced.

3.1.2 Observation of collapsing microbubbles

Fig. 7(a) shows the images of a microbubble interacting with a shock wave obtained by the ultra-high-speed framing camera. The images were obtained using an exposure time 30 ns, frame interval of 450 ns, and an initial bubble diameter of 45 μm. The propagation of the shock wave in the frames is from right to left, and the microbubble interacted with the shock wave between Frames 2 and 3. In Frame 4, a spherical rebound shock wave can be observed around the microbubble. The images suggest that the bubble maintained a spherical shape during contraction. Fig. 7(b) compares the experimentally and analytically determined time variations of the bubble diameter due to the pressure profile of the experimental shock wave. The triangle on the horizontal axis indicates the time at which the bubble contracts to the minimum radius, estimated from the mean propagation speed of the rebound shock wave around the bubble in Frame 4. The results of the numerical analysis using the spherical symmetrical model can be observed to be in good agreement with the experimental results. Furthermore, the predicted pressure attenuation of the rebound shock wave induced by the collapsing microbubble is shown in Fig. 8. The horizontal axis of the figure represents the distance in the radial direction from the center of the microbubble. By the numerical simulation, the maximum pressure of the rebound shock wave front was estimated to be 3333 MPa, after the occurrence of which the bubble re-expanded from the minimum radius to a radius of 3.29 μm. Additionally, the maximum pressure inside the bubble was calculated to be 1130 MPa by Eq. (1). The pressure of the shock wave front decreased exponentially from 3333 MPa with increasing distance from the center. Using the present prediction method, the pressure at the rebound shock wave front in Frame 4 of Fig. 7(a) was estimated to be about 5.49 MPa.

The images of the interaction of a microbubble with a shock wave shown in Fig. 9(a) were taken under the same conditions as those for Fig. 7(a), with the exception of the initial diameter of the microbubble being 48.3 μm. The propagation of the incident shock wave in the frames is from right to left. In Frame 2, the shock wave just passed through the microbubble. In Frame 3, the microbubble began to shrink and a spherical rebound shock wave was generated. In the next frame, it was noticed that the shadow of the expanding microbubble had lost its sphericity, which suggested that a microjet was generated toward the left. It was therefore considered that the collapse generated a non-spherical rebound. Notwithstanding the nonsphericity, the analytical results for this case are compared with those of experiment in Fig. 9(b). The triangle on the horizontal axis indicates the estimated time of the maximum shrinkage of the bubble. It was observed that the experimental bubble motion was slower than the analytical estimation at about 130 ns. The shrinkage and expansion of a non-spherical collapse appear to be unstable, and the internal pressure of the bubble is therefore unable to attain a sufficiently high value, resulting in a slowdown of the overall bubble motion.

Fig. 10 shows the images of a microbubble interacting with a shock wave, obtained by the ultra-high-speed framing camera. The images were obtained using an exposure time of 50 ns, frame interval of 450 ns, and an initial spherical bubble diameter of 48 μm. The shock wave propagation in each frame was from right to left. The microbubble interacted with the shock wave between Frames 1 and 2. Although the images of the bubble shadow are not clear, the bubble in Frame 2 began to deform. Protrusions are discernible on the left side of the microbubble shadow in Frame 3 and Frame 4, suggesting the presence of microjets [10]. This indicated a non-spherical collapse.

When a non-spherical collapse is induced by an underwater shock wave, the generation of strong rebound shock waves is not expected. In order to develop the shock sterilization treatment, it is important to increase the generation probability of spherical collapse of microbubbles. The smaller a microbubble becomes, the larger the surface tension is. Therefore, it is necessary to confirm the collapse behavior of microbubbles smaller than 45 μm.

3.2 Behavior of Microbubbles after Collapse

To understand the interaction of single and multiple microbubbles with a shock wave, a microscopic observation setup was developed as shown in Fig. 11. The experimental setup consisted of a microscope (CKX41, Olympus Co.), a high-speed camera (FASTCAM-SA5, Photoron Co.), a fiber optical probe hydrophone for measuring pressure, a metal halide lamp (LS-M350), a high-voltage pulse discharge power supply, and a test chamber.

Fig. 12 shows the behavior of a single bubble after the first rebound. A ×4 image magnification, 0.369 μs exposure, and 10 μs frame interval were used for the imaging. The propagation of the shock wave in the frames was from left to right. The initial microbubble diameter was 25 μm. A bubble formed a microjet 20 μs after the shock wave passed through it, and then expanded to about 125 μm, eventually breaking after 40 μs. The broken bubbles re-expanded and coalesced after 160 μs to form a single bubble of diameter 20 μm. It was, however, observed that some of the smaller bubbles remained in a cloud-like form around the large bubble.

Fig. 13 shows the behavior of the multiple bubbles after their collapse. The imaging conditions in this case were ×10 magnification, 1 μs exposure, and 10 μs frame interval. The initial diameter of each microbubble was considered to be about 20 μm, and the imaging area was 300 × 200 μm^2. After passage of a shock wave through the bubbles, they flocked around the center of the image and repeatedly expanded and contracted until they coalesced. After 160 μs, the bubbles had coalesced into a single bubble of about 28 μm diameter. It can be seen from the foregoing that complex interaction among the microbubbles continues after their interaction with the shock wave.

4. Conclusion

To establish the method of treating ballast water using interaction between shock waves and microbubbles, experimental observation and numerical analysis of the microbubble behavior during the interaction were conducted. The microbubble motion induced by the underwater shock wave was observed using ultra-high-speed framing cameras and analyzed by a symmetrical one-dimensional spherical model. The pressure attenuation of the shock wave rebound due to microbubble collapse was also estimated using a point-symmetric numerical simulation and the results of the numerical analysis. The analytically determined relationship between the maximum internal pressure of the bubbles and the initial bubble diameter revealed the existence of an optimal bubble diameter range for maximizing the internal pressure for a given shock wave pressure profile. To enhance the experimental observation of the microbubble behavior, positioning control of the bubbles was employed. Magnified observation using the ultra-high-speed framing cameras established the occurrence of rebound shock wave generation, microjet formation, and collapse and re-combination of the bubbles through contraction and expansion. For a bubble that maintained a spherical shape when it collapsed, the time variation of its diameter determined by experiment was observed to be in good agreement with that determined by numerical analysis. Furthermore, the maximum pressure of the spherical rebound shock wave was estimated to be 1172 MPa. Conversely, in the case of non-spherical collapse, the corresponding experimental results differed from those of analysis. It is supposed that spherical collapse produced stronger rebound shock waves, which facilitated the maintenance of the sphericity of the smaller microbubbles owing to the relatively large surface tension. Based on the results of this study, to obtain a high pressure from a microbubble rebound, the motion of bubbles of diameter 20–30 μm should be further investigated. It was also observed that single and multiple microbubbles moved vigorously after their interaction with a shock wave and the latter coalesced into a single bubble within several hundred microseconds.

Acknowledgement
This study was supported by JSPS KAKENHI (Grant Numbers 22360367 and 25630405). The authors would like to express their gratitude to Messrs. Satoshi Matsumura and Akira Hirami of Nac Inc., Messrs. Takaaki Mizushima and Hiroyuki Usui of Nobby Tech. Ltd., and Mr. Katsuhiro Takayama of Photoron Co. for their technical assistance in the visualization processes of the study.

Reference

1. A. Abe, K. Kanai, H. Mimura, S. Nishio, H. Ishida, Study on application of shock waves generated by micro bubbles to the treatment of ships' ballast water, Proc. 26th International Symposium on Shock Waves, pp.869-874, 2007.
2. International Maritime Organization, International Convention For The Control And Management Of Ships' Ballast Water And Sediments, 2004.
3. Class NK, Latest Information of Approval of Ballast Water Management System, 2014.
4. A. Abe, H. Mimura, Sterilization of Ships' Ballast Water, Chapter 11 of Bubble Dynamics and Shock Waves, Edited by C. F. Delale, Shock Wave Science and Technology Reference Library Vol. 8, Springer, pp.339–362, 2013.
5. B. Wolfrum, T. Kurz, R. Mettin, and W. Lauterborn, Shock wave induced interaction of microbubbles and boundaries, *Physics of Fluids*, Vol. 15, No. 10, pp.2916–2922, 2003.
6. C. Herring, *OSRD*, Rep. 236, 1941.
7. S. Fukuda, B. Wan, A. Abe, Analytical estimation of microbubble motion exposed to discontinuous pressure change, Proc. 28th International Symposium on Shock Waves, Part12, pp.909-914, 2012.
8. A. Harten, Implicit total variation diminishing (TVD) schemes for steady-state calculations, *Journal of Computational Physics*, Vol. 57, pp. 327–360, 1985.
9. S. Maeno, J. Wang, S. Fukuda, A. Abe, Observation and Analysis of Microbubble Motion Induced by an Under Water Shock Wave, 29th International Symposium on Shock Waves, No.0246-000026, 2013.
10. Z. Ding, S. M. Gracewski, The behavior of a gas cavity impacted by a weak or strong shock wave, *J. Fluid Mech*. Vol.309, pp. 183–209, 1996

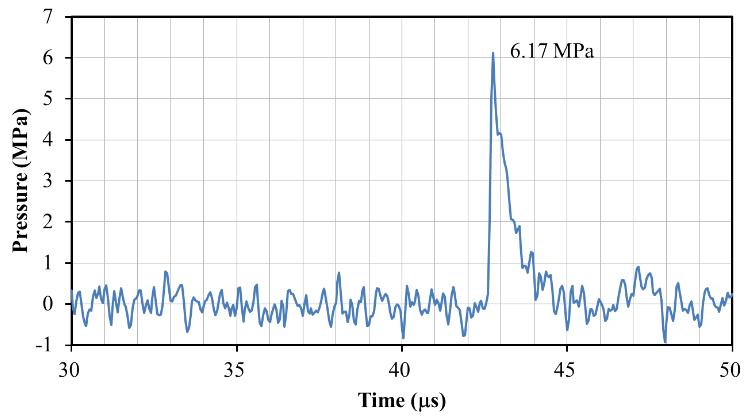

Fig. 1 Pressure profile of an experimental external spherical shock wave measured at 60 mm from the electrical discharge point

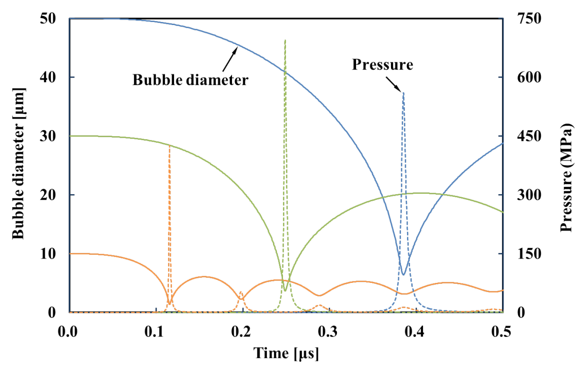

Fig. 2 Time variation of the bubble diameter and internal pressure

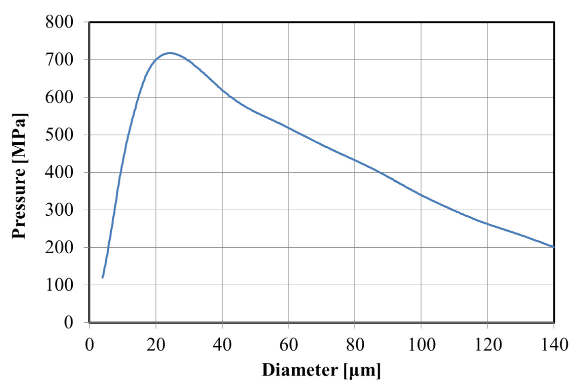

Fig. 3 Maximum internal pressure vs. initial bubble diameter

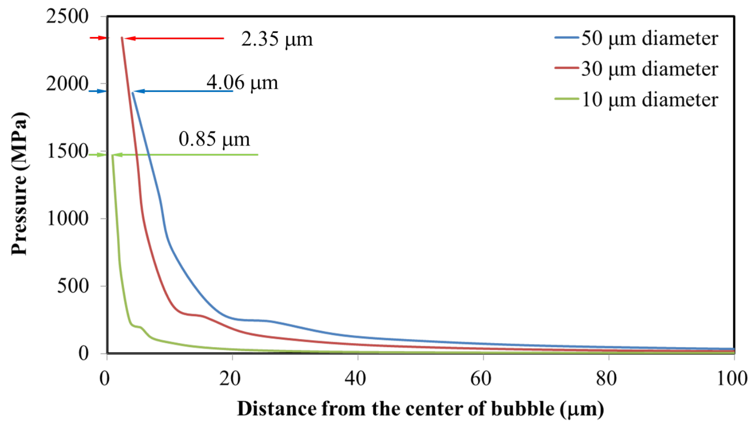

Fig. 4 Pressure attenuation of rebound shock waves generated by collapse motion of microbubbles of diameters 10, 30, and 50 µm

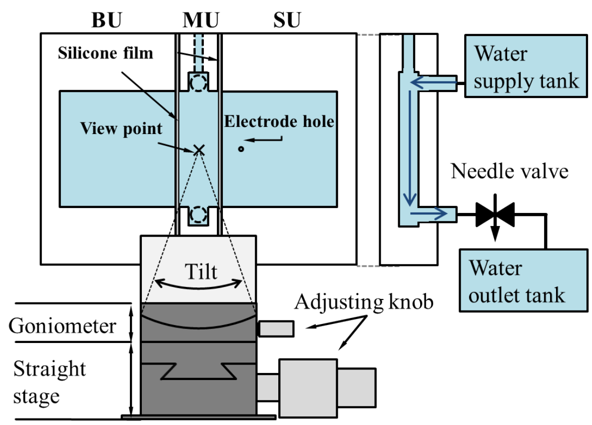

Fig. 5 Schematic diagram of the experimental water tank that comprises three components: the shock wave generation unit (SU), the microbubble position control unit (MU), and the buffer unit (BU).

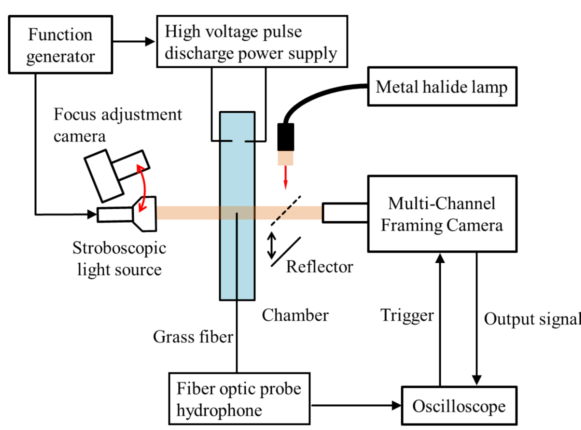

Fig. 6 Schematic diagram of the optical arrangement for visualizing the collapse motion of a microbubble using an ultra-high-speed framing camera

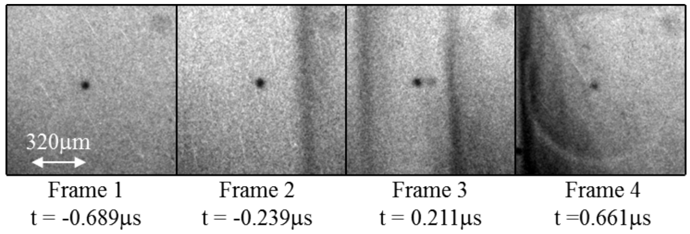

(a)

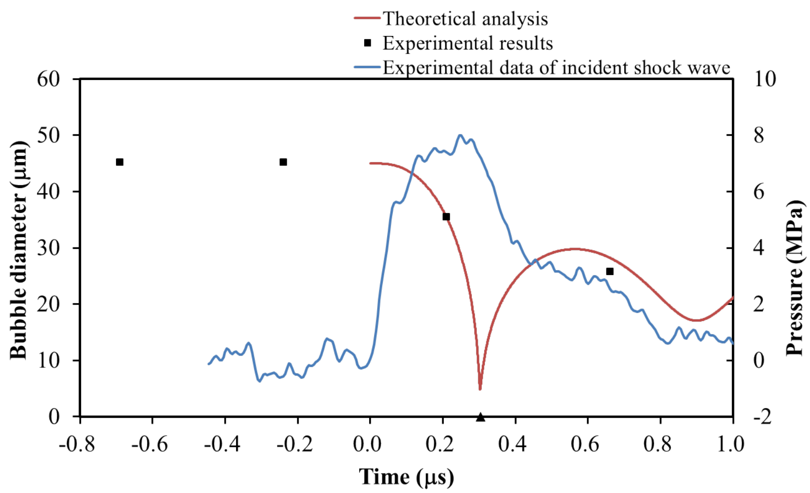

(b)

Fig. 7 Observation of the motion of a microbubble induced by interaction with an underwater shock wave: the initial bubble diameter is 45 µm. (a) Images of the interaction of a microbubble with an underwater shock wave as obtained by the SIM camera. (b) Comparison of the experimentally and analytically determined time variations of the bubble diameter

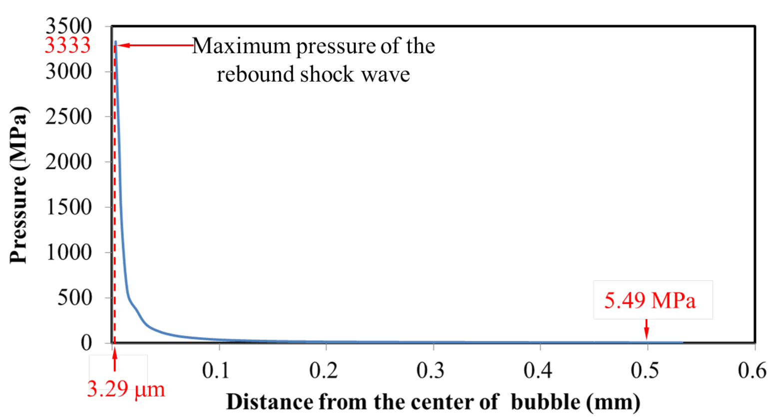

Fig. 8 Numerical analysis of the pressure attenuation of the experimental underwater shock wave due to the rebound shock wave for a microbubble of initial diameter 45 µm exposed to the shock wave

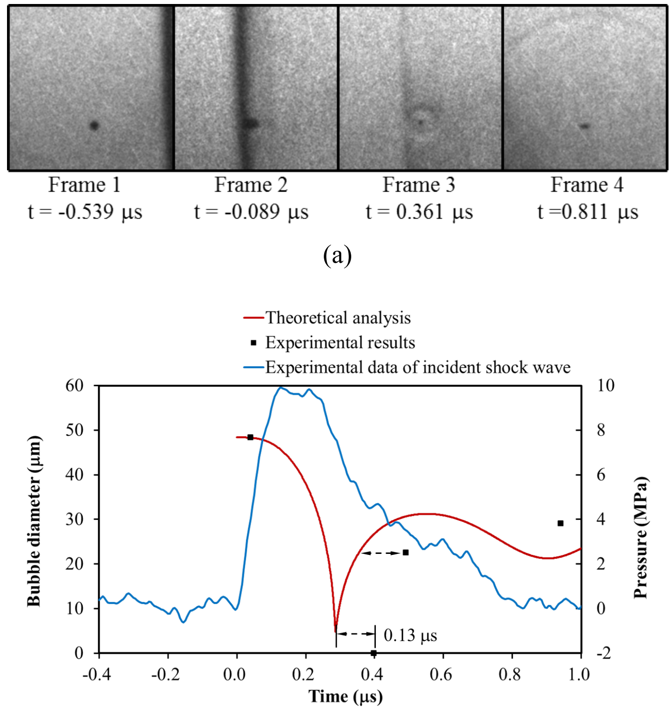

Fig. 9 Observation of microbubble motion induced by interaction with an underwater shock wave: the initial bubble diameter is 48.3 μm. (a) Images of the interaction of a microbubble with an underwater shock wave as obtained by the SIM camera. (b) Comparison of experimentally and analytically determined time variations of the bubble diameter

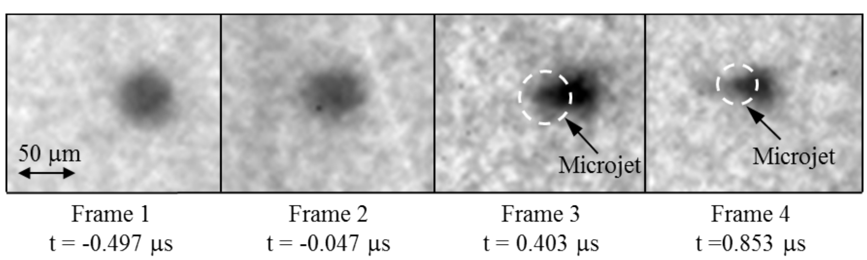

Fig. 10 Images of non-spherical collapse of microbubble induced by a shock wave: the initial bubble diameter is 48.3 μm

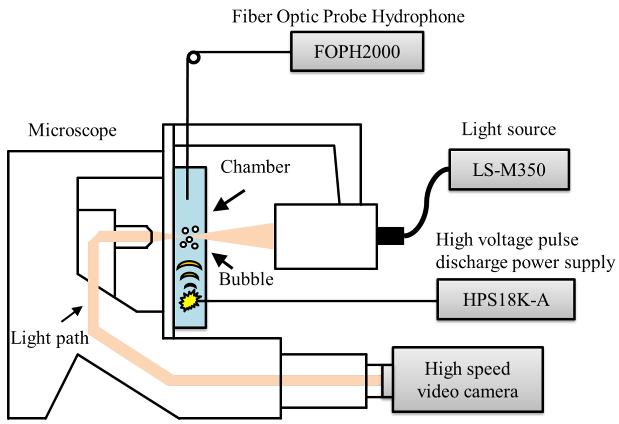

Fig. 11 Microscopic observation setup for the interaction of single and multiple microbubbles with an underwater shock wave

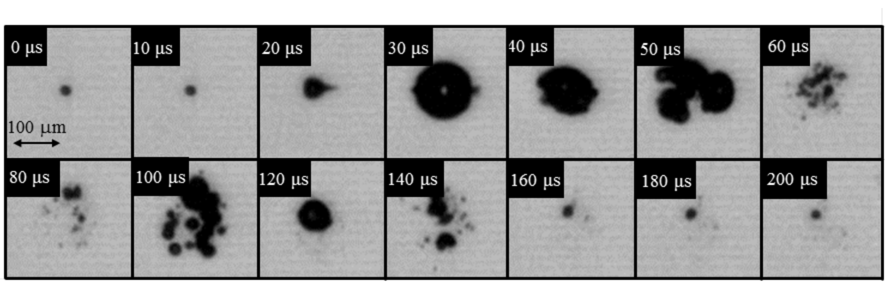

Fig. 12 Behavior of a single microbubble after the first rebound induced by an underwater shock wave

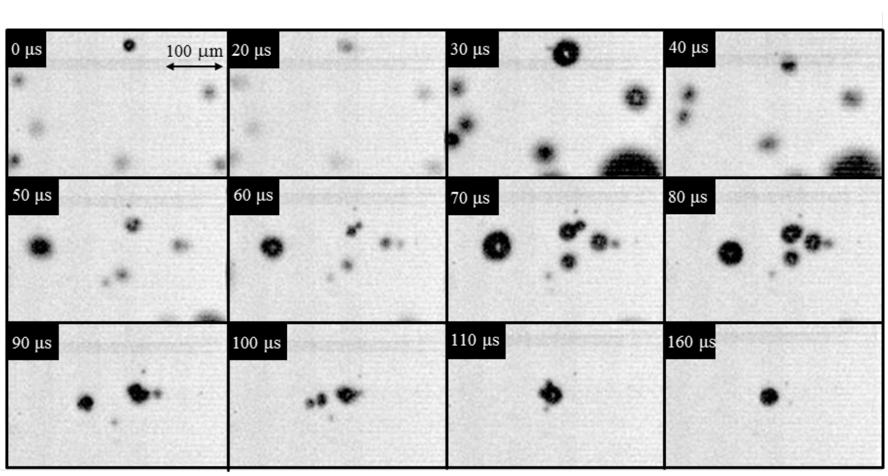

Fig. 13 Coalescent behavior of multiple microbubbles after their collapses induced by an underwater shock wave